



Cite this: *RSC Adv.*, 2018, 8, 13857

Optimizing the performance of photocatalytic H₂ generation for ZnNb₂O₆ synthesized by a two-step hydrothermal method†

Yutong Chun,^a Mufei Yue,^a Pengfei Jiang,^a *^{ab} Shijian Chen,^b  Wenliang Gao,^b 
 Rihong Cong,^a  and Tao Yang,^a *

Semiconductor-based photocatalytic H₂ generation is a promising technique and the development of efficient photocatalysts has attracted great attention. Columbite-ZnNb₂O₆ is a wide-bandgap semiconductor capable of photocatalytic water splitting. Here we employed a two-step hydrothermal method to first dissolve Nb₂O₅ with a highly basic aqueous solution and further react it with Zn²⁺ to form nanosized ZnNb₂O₆. The reaction time plays an important role on its morphology and photocatalytic performance in water reduction. The sample synthesized through 7 days of reaction was the optimal one with an appropriate crystallinity and a large specific surface area, however the severe surficial defects prohibited its photocatalytic activity in pure water. The H₂ generation at a rate of 23.6(5) μmol h⁻¹ g⁻¹ emerged when 20 vol% methanol was used as the hole-sacrificial agent. Most remarkably, once metal or metal oxide cocatalysts, including Pt, Au, NiO, RuO₂, Ag₂O, and Pd/PdO, were loaded appropriately, the photocatalytic H₂ generation rate ultimately achieved 3200(100) or 680(20) μmol h⁻¹ g⁻¹ with or without using methanol, respectively. Apparent quantum yields (AQYs) at 295 nm were investigated by changing the experimental parameters, and the optimal AQYs are 4.54% and 9.25% in water and methanol solution, respectively. Further post-modifications like bandgap engineering may be performed on this highly efficient nano-ZnNb₂O₆.

Received 23rd February 2018
 Accepted 9th April 2018

DOI: 10.1039/c8ra01624k

rsc.li/rsc-advances

Introduction

The technology of semiconductor-based photocatalytic water reduction using solar energy has been considered as one possible solution to the incoming energy crisis. Research on developing new semiconductor photocatalysts is always active.^{1–3} Due to the d¹⁰ electron configuration of Nb⁵⁺, people have developed several niobium-containing oxide photocatalysts, for example, K₄Nb₆O₁₇,^{4,5} Ag₂Nb₄O₁₁,⁶ Ba₅Nb₄O₁₅,⁷ Bi₃NbO₇,⁸ and ZnNb₂O₆.^{9–11}

We are interested in columbite-type ZnNb₂O₆, which was already suggested to be potentially applicable as dielectric ceramics or luminescent materials.^{12–15} The columbite structure of ZnNb₂O₆ is constructed by a distorted hexagonal-closed-packed ionic sub-lattice along the *a*-axis, where half of the octahedral cavities are occupied by either Zn²⁺ or Nb²⁺ in an ordered mode as shown in Fig. S1 in the ESI.† With regards to

its photocatalytic activity in water splitting, A. Kudo reported in 1999 that ZnNb₂O₆ loaded with 0.5 wt% NiO possessed a high activity (54 and 21 μmol h⁻¹ g⁻¹ for H₂ and O₂ production, respectively) under the irradiation of 450 W high pressure mercury lamp.⁹ ZnNb₂O₆ powder catalyst in that study was prepared by typical high temperature solid state reaction, which must be composed of poly-crystallites with the size in the micrometer level.

In 2009, J. S. Lee performed the band structure engineering on ZnNb₂O₆ by doping V⁵⁺ at the Nb⁵⁺ site, in order to acquire the visible light response.¹⁶ Indeed, the bandgap energy was reduced from 3.98 eV at *x* = 0 to 2.5 eV at *x* = 0.06, and the apparent quantum yields were 0.12% and 1.5% for H₂ and O₂ generation at 420 nm, respectively, in aqueous solutions containing sacrificial agents. Very recently, W. D. Shi selected ZnNb₂O₆ to combine with both N-doped graphene quantum dots and g-C₃N₄ to construct a composite catalyst with efficient heterojunctions, and eventually the visible light driven water reduction activity of g-C₃N₄ was significantly boosted.¹⁷

It is well known that the semiconductor-based photocatalytic reaction contains three successive processes after the photons been absorbed, including the formation of the photo-excited electrons and holes, their migration to the particle surface, and the surficial reaction with, for example, water molecules. Particularly, ZnNb₂O₆ is a relatively resistive semiconductor,

^aCollege of Chemistry and Chemical Engineering, Chongqing University, Chongqing 401331, P. R. China. E-mail: pengfeijiang@cqu.edu.cn; taoyang@cqu.edu.cn

^bCollege of Physics, Chongqing University, Chongqing 401331, P. R. China

† Electronic supplementary information (ESI) available: Crystal structure of ZnNb₂O₆, emission spectrum for Hg-lamp, BET curves, time-dependent H₂ generate curves for as-synthesized ZnNb₂O₆ samples and ZnNb₂O₆-7D loaded with various cocatalysts. See DOI: 10.1039/c8ra01624k



and the migration of electrons/holes to the surface is very difficult due to the high resistivity, as a consequence, only the photo-excited electrons and holes formed spatially close to the surface can contribute to the catalytic reactions, while most electrons and holes in the inner part of the bulk crystallites will annihilate inevitably. The strategy to solve this problem is simply preparing nanosized catalysts, which would not only greatly decrease the distance of the migration length to the surface, but also offer a higher specific surface area along with more active sites for catalytic reactions.

Herein this work, Nb_2O_5 was dissolved in the highly basic solution (KOH aqueous solution) in a closed system, and further reacted with Zn^{2+} to form phase-pure ZnNb_2O_6 nanoparticles at hydrothermal conditions. Its band structure was explored by density functional theory calculations, and experimentally, the potentials of valence band maximum and conduction band bottom were estimated by the ultraviolet photoelectron spectroscopy and UV-Vis diffuse reflectance spectra to be 3.5 and -0.47 eV, respectively. The nanosized ZnNb_2O_6 synthesized hydrothermally exhibited a high specific surface area, and with the assistance of the sacrificial agents, it possessed an intrinsic photocatalytic activity in H_2 production under UV light irradiation, however, no activity was detected in pure water, indicating the surficial defects may cause the high recombination rate of electrons and holes. Then, various metal or metal oxide cocatalysts (including Pt, Au, RuO_2 , NiO, Pd/PdO, and Ag_2O , identified by X-ray photoelectron spectroscopy) were deposited on the nanoparticle surface, and the photocatalytic H_2 production rate increased significantly up to 680(20) and 3200(100) $\mu\text{mol h}^{-1} \text{g}^{-1}$ in pure water and methanol aqueous solution, respectively. The high stability of ZnNb_2O_6 was confirmed by cycling experiments and the powder X-ray diffraction after the photocatalysis, in addition, the optimal apparent quantum yields (AQY) under irradiation of the monochromatic light at 295 nm were 4.54% in pure water and 9.25% in 20 vol% methanol aqueous solution, respectively. Our efforts on optimizing the intrinsic photocatalytic performance of ZnNb_2O_6 offers a new platform for further post-modifications, like bandgap engineering or constructing a composite catalyst system.

Experimental

Synthesis of catalyst and loading of cocatalysts

A two-step hydrothermal method was applied to synthesize ZnNb_2O_6 photocatalyst.¹¹ First, a pre-reaction was performed to dissolve Nb_2O_5 (0.10 g) using 7.5 mL of KOH aqueous solution (4 mol L^{-1}) in a closed system at 180 °C for 10 hours. Then a pre-calculated amount of $\text{Zn}(\text{Ac})_2 \cdot 2\text{H}_2\text{O}$ with a molar ratio of Zn : Nb = 1 : 2 was loaded into this solution. Afterwards, pH was adjusted to ~ 6 using concentrated hydrochloric acid under stirring. Finally, a turbid solution will be obtained and further loaded into a 25 mL Teflon-lined autoclave, sealed and kept at 240 °C for 3, 5, 7, and 9 days, respectively. After the reaction, the autoclave was naturally cooled to room temperature. The so-obtained solid product was washed extensively for several times with alcohol and water, and then dried at 60 °C. The

resultant white powder sample was donated as ZnNb_2O_6 -3D, -5D, -7D, -9D, respectively. The comparison sample of bulk- ZnNb_2O_6 was synthesized by typical high temperature solid state reaction. Stoichiometric reagents of ZnO and Nb_2O_5 were mixed and heated at 850 °C for 15 hours.

The loading of cocatalyst was proceed using the reduction method in KBH_4 aqueous solution. Typically, 100 mg of ZnNb_2O_6 catalyst and a pre-calculated amount of metal salt solution ($\text{H}_2\text{PtCl}_6 \cdot 6\text{H}_2\text{O}$, PdCl_2 , $\text{HAuCl}_4 \cdot 4\text{H}_2\text{O}$, AgNO_3 , $\text{Ni}(\text{NO}_3)_2 \cdot 6\text{H}_2\text{O}$, or RuCl_3) was mixed in 50 mL of distilled water. This mixed aqueous solution in a 100 mL beaker was ultrasonicated for 20 minutes. An appropriate amount of diluted KBH_4 aqueous solution was added into the beaker very slowly. Finally, the obtained powder sample was washed extensively with water and dried at 60 °C for further usage.

Characterizations

Powder X-ray diffraction (XRD) data were collected on a PANalytical X'pert diffractometer equipped with a PIXcel 1D detector with Cu $K\alpha$ radiation. The operation voltage and current are 40 kV and 40 mA, respectively. Scanning electron microscopy (SEM) images were taken using a JSM-7800F electron microscope at the voltage of 3 kV and the working distance of 4 mm. The nitrogen adsorption-desorption experiments were performed at 77 K using a Quantachrome Quadrasorb SI analyzer. Prior to measurements, the samples were degassed at 300 °C for 10 hours, and the specific surface area was estimated according to the Brunauer-Emmett-Teller (BET) method. The UV-Vis diffused reflectance spectra (DRS) were recorded at room temperature using a UV-Visible-Near Infrared spectrometer (Shimadzu UV-3600) equipped with an integrating sphere attachment. BaSO_4 was used as reflectance standard. The X-ray photoelectron spectra (XPS) and ultraviolet photoelectron spectroscopy (UPS) were acquired with an Escalab 250xi photoelectron spectrometer with Ag $K\alpha$ X-ray source and Ar $K\alpha$ ultraviolet ray source, respectively. Photoelectrochemical (PEC) measurements were performed in a typical three-electrode electrochemical on a Zahner electrochemical workstation and PP211, in which the ZnNb_2O_6 film on FTO substrate, Pt wire, and Ag/AgCl electrode were used as the working, counter, and reference electrodes, respectively. A 1.0 M Na_2SO_4 aqueous solution was used as the supporting electrolyte to maintain the stability of the film. The light irradiation was obtained from a monochromatic light ($\lambda = 365$ nm).

Theoretical calculations

Theoretical studies were operated by the Vienna *ab initio* simulation package (VASP).¹⁸ The projector augmented-wave (PAW) method¹⁹ implemented in the VASP code was utilized to describe the interaction between the ionic cores and the valence electrons. The generalized gradient approximation (GGA) parameterized by Perdew, Burke, and Ernzerhof (PBE)²⁰ was employed to describe the exchange-correlation potential in the standard Density Function Theory (DFT) calculations. For single point energy and density of states, a cutoff energy of 500 eV for the plane-wave basis and $7 \times 7 \times 7$ Monkhorst-Pack



G-centered k -point meshes were employed. The band structures $E(k)$ were computed on a discrete k mesh along with high-symmetry directions.

Photocatalytic activity evaluation

Photocatalytic H_2 production was tested on a gas-closed circulation system equipped with a vacuum line (CEL-SPH2N system), a 150 mL Pyrex glass reactor with a quartz cover, and a gas sampling port that is directly connected to a gas chromatograph (Shanghai Techcomp-GC7900, TCD detector, molecular sieve 5A, N_2 gas carrier). In a typical run, 50 mg of catalyst was dispersed by a magnetic stirring bar in 50 mL of pure water or 20 vol% methanol aqueous solution. A 5 °C recycling water bath was applied to keep the reaction vessel at a constant temperature. The irradiation source was generated by an external 500 W high-pressure mercury lamp laid on the top of the reaction vessel, whose emission spectrum is provided in Fig. S2, ESI.†

The apparent quantum yield (AQY) for H_2 evolution under a monochromatic irradiation of 295 nm was calculated according to the following equation.

$$AQY = \frac{\text{number of reacted electrons}}{\text{number of incident photons}} \times 100$$

The number of reacted electrons is related to the H_2 production rate, and the number of incident photons can be calculated according to the beam intensity measured by the Si-photodiode.

Results and discussion

Synthesis and morphology

The two-step hydrothermal method has the advantage in dissolving Nb^{5+} into the basic aqueous solution, and is beneficial for the preparation of nanosized crystallites in comparison with the traditional solid state reaction. The pH value, reaction temperature, and most importantly the reaction time strongly affect the purity and morphology of the final product. In literature, only the powder sample of $ZnNb_2O_6$ prepared at hydrothermal condition for 5 days was studied using the model reaction of photocatalytic degradation for methylene blue.¹⁴

Herein this study, the powder products with the reaction times of 3, 5, 7, and 9 days were collected and characterized by XRD, SEM and BET analyses. As shown in Fig. 1, all the XRD patterns are consistent with the standard one of $ZnNb_2O_6$ (JCPDS No. 76-1827), indicating the phase purity. Some evolution tendency can be observed by comparing these four patterns. For instance, all the peaks in the sample $ZnNb_2O_6$ -3D are broad. This is usually originated from the low crystallinity of the particles, which is reasonable due to the short reaction time of 3 days. For $ZnNb_2O_6$ -5D, all the peaks become more obvious, but they can be classified into two groups. The first group comprises the broad peaks, as represented by two strong peaks with the indices of (310), (311), while the peaks with the indices of (002), (021), (600), (602) and (621) are relatively sharp,

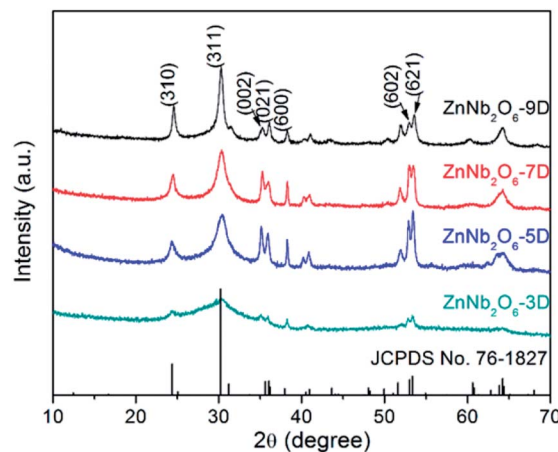


Fig. 1 XRD patterns of $ZnNb_2O_6$ obtained by hydrothermal method for 3, 5, 7 and 9 days.

belonging to the second group. In a single-phase sample, the observable difference in peak shape is probably caused by the structural disordering and/or anisotropic crystal growth, and the latter one will result into low dimensional crystallites in morphology, *i.e.* needle- or petal-like. With further increasing the reaction time to 9 days, the difference in width between these two groups of peaks become smaller.

The evolution deduced from powder XRD patterns could be visualized directly by SEM images. As shown in Fig. 2, small nanoparticles with the size well below 100 nm aggregated when the reaction stopped after 3 days, and with the increasing of the reaction time, petal-like crystallites emerged and became the major component in $ZnNb_2O_6$ -7D, however, the petal-like morphology generally disappeared in $ZnNb_2O_6$ -9D due to the sufficient crystal growth. Accordingly, the specific surface area estimated using BET method exhibited a decreasing tendency from 101, 82, 61 to 41 $m^2 g^{-1}$ for 3D, 5D, 7D, and 9D samples, respectively (see Fig. S3, ESI†).

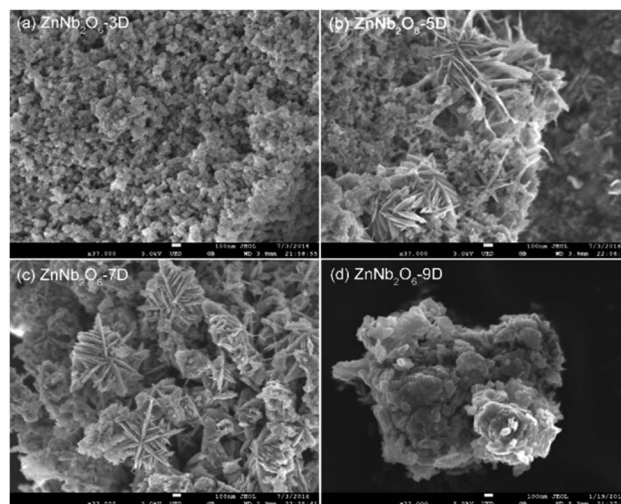


Fig. 2 SEM images of (a) $ZnNb_2O_6$ -3D, (b) $ZnNb_2O_6$ -5D, (c) $ZnNb_2O_6$ -7D and (d) $ZnNb_2O_6$ -9D.



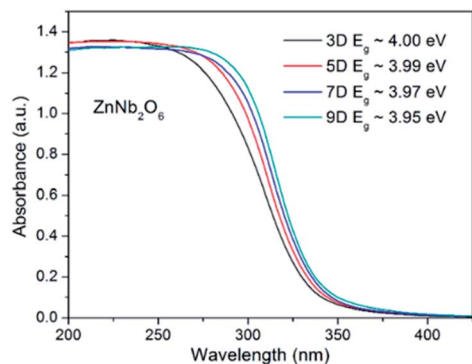


Fig. 3 UV-Vis reflectance spectra of ZnNb_2O_6 -3D, -5D, -7D, and -9D. The bandgap energies provided here were estimated from their differential curves.

Light harvesting ability and band structure analysis

Light harvesting is the first stage of photocatalysis, and the UV-Vis diffuse reflectance spectra for all four ZnNb_2O_6 samples were provided in Fig. 3. An obvious smooth and steep edge can be seen with only slight differences among these samples, which is an indication of the typical semiconducting-type bandgap transition. The bandgap energy, estimated by the negative peak at the differentiate curves, was 3.95, 3.97, 3.99, and 4.00 eV, for ZnNb_2O_6 -9D, 7D, 5D, and 3D, respectively. One possible explanation to the slight increase in bandgap energy

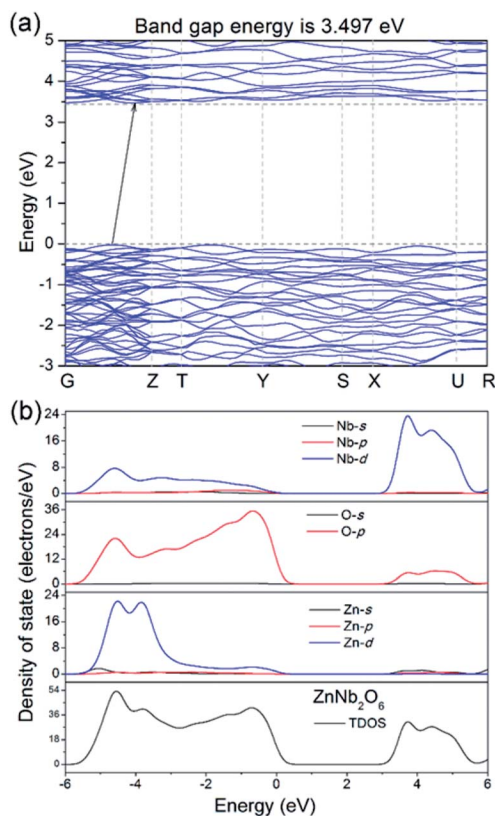


Fig. 4 (a) Calculated energy band structure of ZnNb_2O_6 , (b) partial and total density of state in the range from -6 to 6 eV.

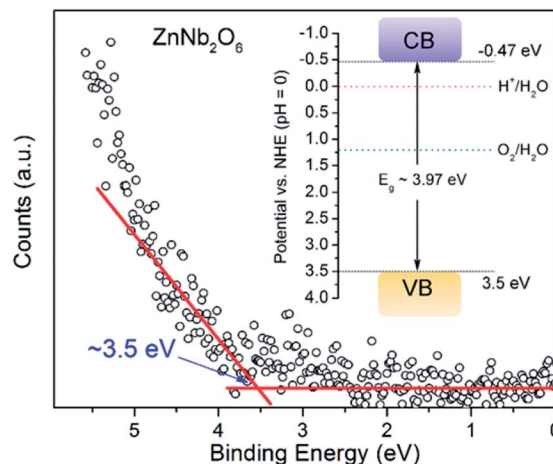


Fig. 5 Potential of valence electron for ZnNb_2O_6 was estimated according to the rising point in ultraviolet photoelectron spectrum, and the proposed band structure potentials are provided as the inset.

from ZnNb_2O_6 -9D to ZnNb_2O_6 -3D is the quantum effect, as can be seen in the SEM images.

DFT calculations help the understanding of the band structure and the possible electronic conduction mechanism. As shown in Fig. 4a, it is an indirect semiconductor with the

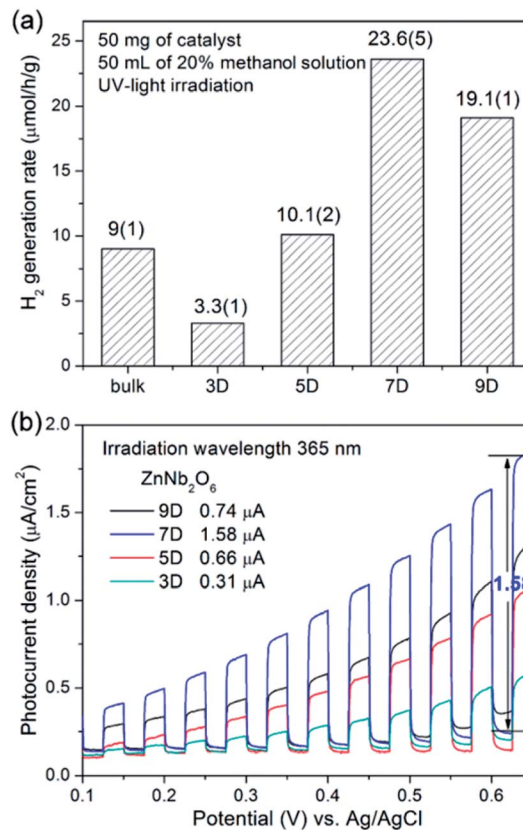


Fig. 6 (a) Photocatalytic H_2 generation rates of bulk- ZnNb_2O_6 and nano- ZnNb_2O_6 synthesized hydrothermally for 3, 5, 7, and 9 days, (b) photoelectrochemical responses using a three-electrode setup in 0.1 M Na_2SO_4 aqueous solution.



calculated bandgap energy of 3.497 eV, smaller than the estimated ones by DRS spectra, which is commonly seen due to the discontinuity of the XC energy during the calculations. In addition, the calculated partial density states (PDOS) in Fig. 4b indicates that the top of the valence band (VB) is dominated by O 2p orbitals, while the bottom of the conduction band (CB) is mainly dominated by the Nb 5d orbitals. This is understandable and it suggests that the electronic conduction is mainly dominated by the Nb–O covalent bonds, *i.e.* photo-excited electrons/holes probably move along the NbO₆ octahedra-based zig-zag chains.

Apparently, both potentials for VB and CB of ZnNb₂O₆ are sufficient for the water oxidation and reduction, respectively, since the water splitting activity has been reported in literature.⁹ Here, ultraviolet photoelectron spectroscopy (UPS) was applied to acquire the actual potential of the valence electron. We propose that the VB potential is roughly 3.5 eV according to Fig. 5. In combination with the experimental value of bandgap energy from DRS (*i.e.* 3.97 eV), the CB potential is −0.47 eV (see the inset of Fig. 5).

In order to further corroborate the correctness of these values, a semi-empirical calculation based on Mulliken electronegativity²¹ was performed using the following equations:

$$E_{\text{VB}} = \chi - E_{\text{c}} + 1/2E_{\text{g}} \quad (1)$$

$$E_{\text{CB}} = E_{\text{VB}} - E_{\text{g}} \quad (2)$$

E_{VB} and E_{CB} are potentials of VB and CB edges, respectively. χ is Mulliken electronegativity, which is 6.18 eV according to its formula. E_{c} is the energy of free electrons on the hydrogen scale (4.5 eV). E_{g} is band gap value obtained from the DRS (*i.e.* 3.97 eV). Accordingly, the as-estimated E_{VB} and E_{CB} are 3.665 eV and −0.305 eV, which are generally consistent with the obtained values from the UPS method.

Photocatalytic performances of as-synthesized ZnNb₂O₆

Under UV irradiation, all four as-synthesized samples (ZnNb₂O₆-3D, -5D, -7D, and -9D) as well as the bulk-type ZnNb₂O₆ obtained from high temperature solid state reaction were active to catalyze the H₂ generation with the assistance of methanol (20 vol%) as the sacrificial agent. As shown in Fig. 6a, the hydrothermal samples exhibited the optimal activity of 23.6(5) $\mu\text{mol h}^{-1} \text{g}^{-1}$, while the H₂ generation rate of the bulk ZnNb₂O₆ was 9(1) $\mu\text{mol h}^{-1} \text{g}^{-1}$. Time-dependent H₂ evolution data are provided in Fig. S4, ESI.† First, the performance of nano-type ZnNb₂O₆ was in the same level with the bulk-type sample, although we claimed the great superiority of nano-materials for photocatalysis. Indeed, the nano-type samples all have very large BET surfaces, however, the probably insufficient crystal growth due to the relatively low reaction temperature will

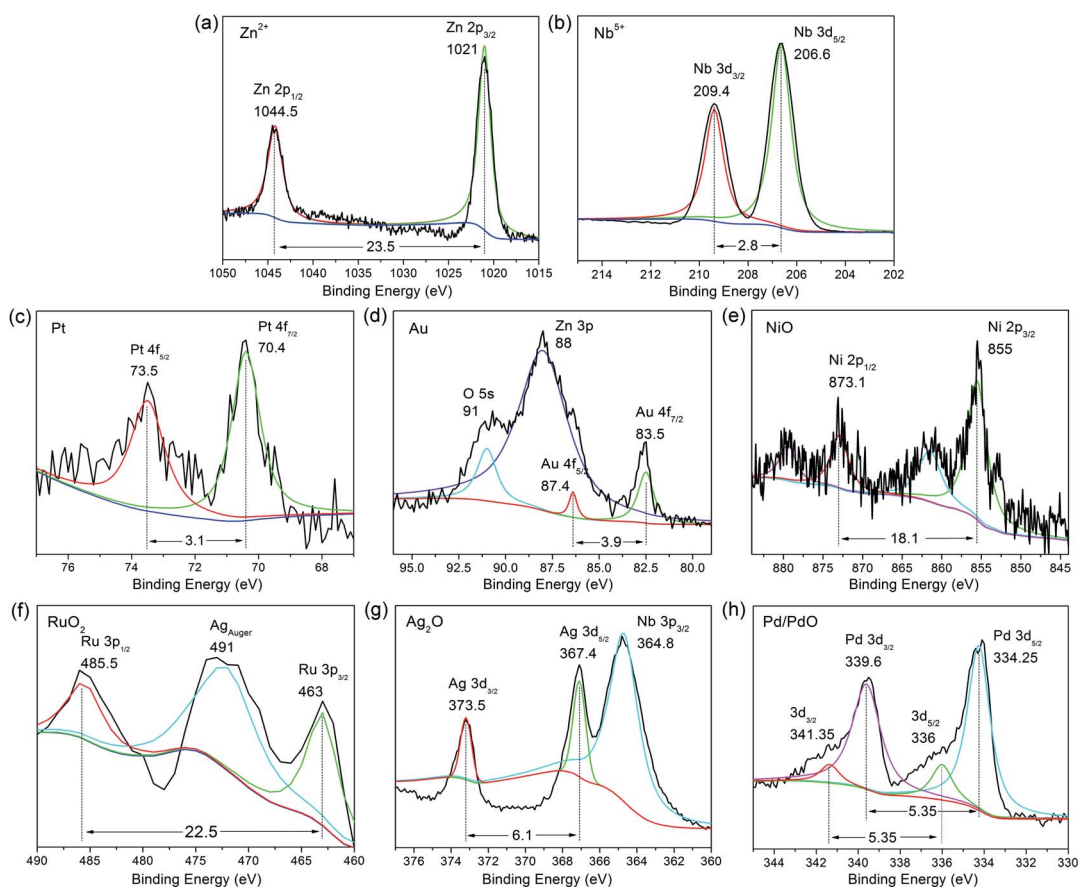


Fig. 7 XPS spectra for (a and b) ZnNb₂O₆ loaded with (c) Pt, (d) Au, (e) NiO, (f) RuO₂, (g) Ag₂O, and (h) Pd/PdO.



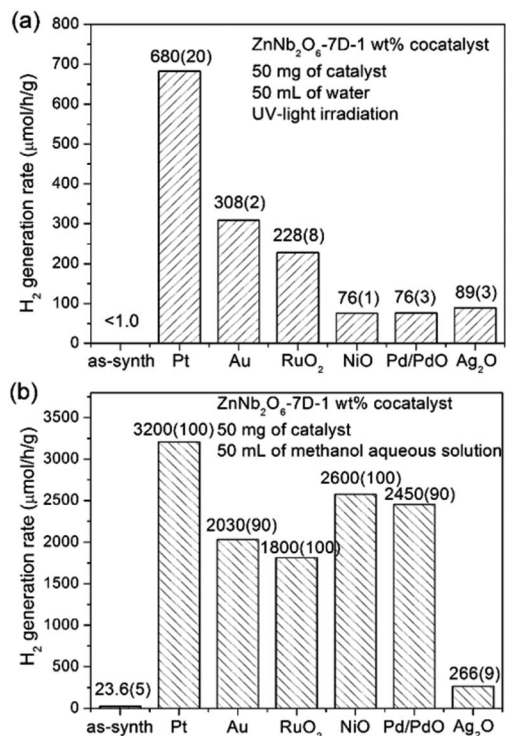


Fig. 8 Photocatalytic H₂ evolution rates of ZnNb₂O₆-7D loaded with 1 wt% co-catalyst in (a) pure water, (b) 20 vol% methanol solution under UV light irradiation.

lead to a large number of surficial defects, *i.e.* the ionic vacancies on the surface, which could be the electron-hole recombination centers. In synthetic chemistry, we could extend the reaction time to overcome this drawback partially. According to SEM and BET experiments, the increase of the crystallinity will decrease the specific surface area. Eventually, ZnNb₂O₆-7D possesses the highest performance under current conditions. This claim could be also proved by the photocurrent measurements in the external electric field, which is a well-known method to understand the generation, separation, and migration of photo-excited charges of semiconductors.^{22,23} As shown in Fig. 6b, the photocurrents of as-prepared ZnNb₂O₆ were recorded in dark with a set of chopped linear-sweeps with a scan rate of 10 mV s⁻¹ between 0.0–0.65 V in 0.1 M Na₂SO₄ solution. The photocurrent responses also exhibited a maximum value for the sample ZnNb₂O₆-7D. Accordingly, it was selected as the best sample in quality for the following experiments.

Cocatalysts loading on ZnNb₂O₆-7D

As mentioned above, the major problem of the nano-ZnNb₂O₆ is the high level of surficial defects, which first could be partially relieved by extending the reaction time. On the other hand, the most commonly used strategy is to post-modify the catalyst powder with specific cocatalysts, *i.e.* metal or metal oxides. It is well known that appropriate loading of co-catalyst on the photocatalysts not only facilitates the surficial charge separation but also offering a large number of catalytic sites, both are positive effects to photocatalysis.²⁴

Six commonly used elements were selected (including Pt, Au, Ru, Ni, Pd, Ag)^{25–30} to be deposited on the surface of ZnNb₂O₆-7D in quantity of 1 wt%. The successful loading and the valence states of these elements were investigated by X-ray photoelectron spectroscopy, which is a useful surface-detecting technique. As expected, Zn²⁺ and Nb⁵⁺ are in their usual valence states as shown in Fig. 7a and b. For instance, Zn 2p level split into two peaks of Zn 2p_{3/2} and Zn 2p_{1/2} due to spin-orbital coupling, which are positioned at 1021 and 1044.5 eV, respectively. It is the same with Nb 3d level, *i.e.* Nb 3d_{5/2} and Nb 3d_{3/2} locate at 206.6 and 209.4 eV respectively. The signals for the loaded elements are detectable but very weak. As shown in Fig. 7c–h, the cocatalysts are supposed to be Pt, Au, NiO, RuO₂, Ag₂O, respectively. The case of Pd is somehow different, where the coexistence of Pd and PdO is proposed on the basis of its peak broadening of the binding energy.

The photocatalytic H₂ generation performances of ZnNb₂O₆-7D loaded with 1 wt% cocatalysts either in pure water or in 20 vol% methanol aqueous solution are presented in Fig. 8. Detailed time-dependent H₂ evolution data are provided in Fig. S5, ESI.† First, the photocatalytic activity of as-prepared ZnNb₂O₆-7D was almost undetectable (<1 μmol h⁻¹ g⁻¹) in pure water, while it increased to 23.6(5) μmol h⁻¹ g⁻¹ when using methanol as the sacrificial agent. This increase is due to the fast consuming of surficial holes by methanol, which, in some content, decreases the recombination rate of surficial charges. Second, the employment of cocatalysts is extremely helpful to enhance the photocatalytic H₂ generation efficiency. The H₂ generation rate achieved up to 680(20) and 3200(100) μmol h⁻¹ g⁻¹ in pure water or methanol aqueous solution when loading with 1 wt% Pt. Additional experiments were performed to find the optimal loading content of Pt. The colour of Pt-loaded samples turned from white to light grey, and finally to dark grey when increasing the weight percentage of Pt up to 2.0 wt%. The sample with 1 wt% Pt exhibited the optimal photocatalytic activity both in pure water and in methanol aqueous solution (see Fig. S6, ESI†). It is proposed that the overabundant co-catalyst would result in large and aggregated Pt particles, thus the light absorbance and the number of effective catalytic sites would decrease. Here in our experiments, the optimal H₂ generate rate can be achieved when the loading content of Pt is 1 wt%.

Apparent quantum yields

Our intention is to explore the potential of ZnNb₂O₆ in photocatalytic water splitting when synthesized as nanomaterials. It is agreed that the photocatalytic H₂ generation efficiency could be affected by the experimental conditions, thus people prefer to use a semi-quantitative parameter, the apparent quantum yield (AQY), to evaluate the photocatalytic efficiency of a specific catalyst. It is a semi-quantitative parameter because people cannot obtain an accurate number of absorbed photons. Practically, we need to adjust the experimental conditions to get an optimal AQY value, such as the quantity of the photocatalyst and aqueous solution, and the beam intensity of the irradiation light. Under the monochromatic incident beam of 295 nm, the



Table 1 Calculated AQYs of ZnNb₂O₆-7D-1 wt% Pt in pure water when varying the dose of catalyst and the volume of water

Light intensity (mW cm ⁻²)	Catalyst (mg)	Water (mL)	H ₂ generation rate (μmol h ⁻¹)	AQY (%)
2.298	50	50	2.4(2)	1.18
	60	50	1.9(1)	0.93
	60	60	2.6(3)	1.29
	70	60	3.4(3)	1.67
	70	70	3.3(3)	1.65
	80	70	4.3(4)	2.14
	80	80	5.6(4)	2.79
	90	80	4.8(4)	2.38
	90	90	3.9(3)	1.95
	100	90	6.2(8)	3.07
	100	100	5.5(5)	2.76
	110	100	9.1(6)	4.54
	110	110	7.8(5)	3.91
	120	110	9(1)	4.41
	140	110	5.4(7)	2.72

Table 2 Calculated AQYs of ZnNb₂O₆-7D-1 wt% Pt in pure water by changing the incident light density

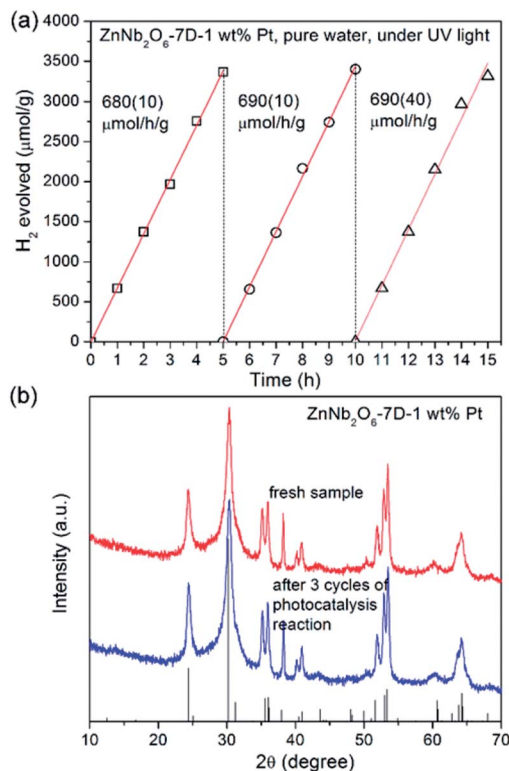
Light intensity (mW cm ⁻²)	Catalyst (mg)	Water (mL)	H ₂ generation rate (μmol h ⁻¹)	AQY (%)
1.335	110	100	3.9(5)	3.35
2.298	110	100	9.1(6)	4.54
3.353	110	100	7.2(9)	2.47

H₂ evolution rates as well as the AQYs are provided in Table 1, where the dosage of the catalyst (ZnNb₂O₆-7D loaded with 1 wt% Pt) as well as the volume of water are variable. A maximal AQY value of 4.54% was obtained when using 110 mg of catalyst and in 100 mL of pure water. When varying the incident beam intensity, the AQY of 4.54% remained the optimal in pure water (see Table 2). In the following, we obtained the highest AQY of 9.25% with the assistance of methanol as the sacrificial agent (see Table 3 for detailed experimental condition).

Finally, the stability of photocatalytic activity and the integrity of the sample crystallinity is very important for a heterogeneous catalyst. As shown in Fig. 9, the photocatalytic activity of ZnNb₂O₆-7D loaded with 1 wt% Pt remained constant for at least three cycles of photocatalytic experiments (15 hours of irradiation). Moreover, the XRD collected for the recovered

Table 3 Calculated AQYs of ZnNb₂O₆-7D-1 wt% Pt in 20 vol% methanol aqueous solution by changing the incident light intensity

Light intensity (mW cm ⁻²)	Catalyst (mg)	20 vol% methanol aq. (mL)	H ₂ generation rate (μmol h ⁻¹)	AQY (%)
0.659	110	100	4.5(3)	7.80
1.998	110	100	16(2)	9.25
4.319	110	100	28(3)	7.45

**Fig. 9** (a) Time-dependent H₂ evolution curves for ZnNb₂O₆-7D-1 wt% Pt in pure water. After each 5 hours, the photocatalysis system was evacuated. (b) XRD patterns for fresh ZnNb₂O₆-7D-1 wt% Pt and the recovered sample after 15 hours photocatalysis experiment.

sample exhibited an identical pattern with the fresh sample, indicating that there was no photo-corrosion under our experimental condition.

Conclusions

The two-step hydrothermal method was employed to synthesize flower-like nanosized ZnNb₂O₆ in order to enhance its photocatalytic performance in water reduction. Experimentally, ZnNb₂O₆-7D exhibited the optimal photocatalytic performance among the samples synthesized hydrothermally with different reaction times, due to its appropriate crystallinity and high specific surface area, for example, the photocatalytic H₂ generation rate was 23.6(5) μmol h⁻¹ g⁻¹, which is indeed larger than that of bulk-ZnNb₂O₆ under the same catalytic condition. However, the drawback of the nano-ZnNb₂O₆ is also very obvious, that is the severe surficial defects due to the low preparation temperature. Consequently, various cocatalysts, including Pt, Au, NiO, RuO₂, Ag₂O, Pd/PdO, were deposited on the catalyst surface by reduction method using KBH₄ solution. It is impressive that the H₂ generation rate increased for two orders, that is 680(20) and 3200(100) μmol h⁻¹ g⁻¹ in pure water and in methanol aqueous solution, respectively. A systematic investigation of AQYs for ZnNb₂O₆-7D-1 wt% Pt was performed by varying the experimental conditions, and the optimal AQYs were 4.54% and 9.25% in water and in methanol solution, respectively.



Conflicts of interest

There are no conflicts to declare.

Acknowledgements

This work was financially supported by the National Natural Science Foundation of China (21671028, 21771027), and Natural Science Foundation of Chongqing (CSTC2016jcyjA0291). We also acknowledge the support from the sharing fund of large-scale equipment of Chongqing University (201712150076).

Notes and references

- 1 A. J. Bard and M. A. Fox, *Acc. Chem. Res.*, 1995, **28**, 141–145.
- 2 A. Kudo and Y. Miseki, *Chem. Soc. Rev.*, 2009, **38**, 253–278.
- 3 X. B. Chen, S. H. Shen, L. J. Guo and S. S. Mao, *Chem. Rev.*, 2010, **110**, 6503–6570.
- 4 T. Takata, A. Tanaka, M. Hara, J. N. Kondo and K. Domen, *Catal. Today*, 1998, **44**, 17–26.
- 5 A. Iwase, H. Kato and A. Kudo, *Catal. Lett.*, 2006, **108**, 7–10.
- 6 X. G. Kong, Z. L. Guo, Q. Lu, J. F. Huang and L. Y. Cao, *J. Alloys Compd.*, 2016, **686**, 48–54.
- 7 Y. Miseki, H. Kato and A. Kudo, *Chem. Lett.*, 2006, **35**, 1052–1053.
- 8 Z. H. Ai, W. K. Ho and S. C. Lee, *Appl. Surf. Sci.*, 2012, **263**, 266–272.
- 9 A. Kudo, S. Nakagawa and H. Kato, *Chem. Lett.*, 1999, **11**, 1197–1198.
- 10 W. M. Wu, S. J. Liang, Z. X. Ding, H. R. Zheng and L. Wu, *Solid State Sci.*, 2011, **13**, 2019–2023.
- 11 X. Huang, Y. Jing, J. Yang, J. Ju, R. H. Cong, W. L. Gao and T. Yang, *Mater. Res. Bull.*, 2014, **51**, 271–276.
- 12 H. J. Lee, K. S. Hong and S. J. Kim, *Mater. Res. Bull.*, 1997, **32**, 847–855.
- 13 R. C. Pullar, *J. Am. Ceram. Soc.*, 2009, **92**, 563–577.
- 14 R. Wang, W. Zhang, Y. L. Xu and L. L. Xing, *Opt. Laser Technol.*, 2014, **58**, 52–55.
- 15 F. W. Mo, L. Y. Zhou, Q. Pang, Y. W. Lan and Z. J. Liang, *Curr. Appl. Phys.*, 2013, **13**, 331–335.
- 16 S. M. Ji, S. H. Choi, J. S. Jang, E. S. Kim and J. S. Lee, *J. Phys. Chem. C*, 2009, **113**, 17824–17830.
- 17 M. Yan, Y. Q. Hua, F. F. Zhu, L. Sun, W. Gu and W. D. Shi, *Appl. Catal., B*, 2017, **206**, 531–537.
- 18 G. Kresse and D. Joubert, *Phys. Rev. B*, 1999, **59**, 1758–1775.
- 19 P. E. Blochl, *Phys. Rev. B*, 1994, **50**, 17953–17979.
- 20 J. P. Perdew, K. Burke and M. Ernzerhof, *Phys. Rev. Lett.*, 1996, **77**, 3865–3868.
- 21 J. J. Liu, X. L. Fu, S. F. Chen and Y. F. Zhu, *Appl. Phys. Lett.*, 2011, **99**, 191903.
- 22 C. Y. Yang, Z. Wang, T. Q. Lin, H. Yin, X. J. Lü, D. Y. Wan, T. Xu, C. Zheng, J. H. Lin, F. Q. Huang, X. M. Xie and M. H. Jiang, *J. Am. Chem. Soc.*, 2013, **135**, 17831–17838.
- 23 T. Hisatomi, J. Kubota and K. Domen, *Chem. Soc. Rev.*, 2014, **43**, 7520–7535.
- 24 J. R. Ran, J. Zhang, J. G. Yu, M. Jaroniec and S. Z. Qiao, *Chem. Soc. Rev.*, 2014, **43**, 7787–7812.
- 25 K. F. Wu, H. M. Zhu, Z. Liu, W. R. Córdoba and T. Q. Lian, *J. Am. Chem. Soc.*, 2012, **134**, 10337–10340.
- 26 M. Murdoch, G. I. N. Waterhouse, M. A. Nadeem, J. B. Meston, M. A. Keane, R. F. Howe, J. Llorca and H. Idriss, *Nat. Chem.*, 2011, **3**, 489–492.
- 27 M. Hara, J. Nunoshige, T. Takata, J. N. Kondo and K. Domen, *Chem. Commun.*, 2003, 3000–3001.
- 28 C. T. Dinh, M. H. Pham, F. Kleitz and T. O. Do, *J. Mater. Chem. A*, 2013, **1**, 13308–13313.
- 29 X. L. Li, P. F. Jiang, M. F. Yue, R. H. Cong, W. L. Gao and T. Yang, *Inorg. Chem.*, 2016, **55**, 1527–1534.
- 30 S. Onsuratoom, T. Puangpetch and S. Chavadej, *Chem. Eng. J.*, 2011, **173**, 667–675.

